RSC Advances

ROYAL SOCIETY OF CHEMISTRY

PAPER

View Article Online
View Journal | View Issue

Check for updates

Cite this: *RSC Adv.*, 2026, **16**, 25197

Magnetite-functionalized eggshell membrane composite: a high-performance magnetic adsorbent for Congo red dye

Faheem Shah *

Received 19th February 2026
Accepted 16th April 2026

DOI: 10.1039/d6ra01484d

rsc.li/rsc-advances

This study develops a sustainable magnetic adsorbent, Fe_3O_4@ESM, by embedding magnetite nanoparticles onto an avian eggshell membrane (ESM) matrix for the efficient remediation of Congo red (CR) from wastewater. Characterization of the functionalized sorbent confirmed a mesoporous structure with a high surface area and abundant binding groups. Zeta potential analysis guided pH optimization. Multivariate optimization was used to identify the optimal conditions for experimental parameters. Under optimum conditions, the proposed sorbent exhibited a high adsorption capacity of 45.04 mg g^{-1}, achieving >96% CR removal. Isotherm and kinetic studies best fitted the Langmuir and pseudo-second-order models, respectively, indicating monolayer, chemisorption-dominated uptake. Thermodynamic studies confirmed a spontaneous, exothermic process with increased interface randomness. The magnetic core enabled simple post-adsorption separation. This work successfully transformed abundant biowaste into high-performance sorbents for sustainable dye removal from wastewater.

Introduction

The emergency of water pollution due to wastewater discharge from industries, such as textiles, printing, and cosmetics, poses a significant risk to global ecosystems.[1] Synthetic dyes represent a constant and hazardous class of contaminants.[2] Azo dyes, characterized by one or more azo bonds (–N=N–), constitute the main and most widely utilized class of dyes.[3] These dyes cause severe aesthetic pollution and impede sunlight penetration, disrupting photosynthetic processes, thus leading to the depletion of dissolved oxygen in aquatic systems. Furthermore, many azo dyes along with their degradation products, especially aromatic amines (*i.e.*, benzidine), are toxic with known mutagenic and carcinogenic effects.[4,5]

Congo red (CR) is a member of the classic anionic azo dyes and a prominent example of this environmental challenge. It has a stable and complex molecular structure with high solubility in water. These properties make it resistant to traditional degradation techniques.[6,7] The presence of CR in water bodies raises a serious concern because it potentially metabolizes into benzidine, known for its carcinogenicity in human beings. Consequently, the development of efficient techniques for the removal of CR from wastewater is a matter of high priority in environmental remediation.[8,9]

Adsorption is one of the excellent techniques for the removal of dyes, due to its high efficacy, cost-effectiveness and simplicity. The quest for best adsorbents has led chemists to explore a variety of materials, such as activated carbon and advanced polymeric resins.[10,11] Likewise, green chemistry principles promote the conversion of biowaste into value-added products. Avian eggshells are abundant waste products from households and food industries and could present an exclusive opportunity in this regard.[12] The eggshell has a calcified structure composed of complex bio-composites with an underlying proteinaceous membrane, which is often discarded.[13] The eggshell membrane (ESM) is a specifically promising material with a fibrous, porous network of proteinaceous structures, such as collagen and keratin, which are rich with amino, carboxyl, and hydroxyl functionalities.[14] These functionalities behave like strong binding sites for pollutant molecules, specifically anionic dyes like CR, through hydrogen bonding, electrostatic attraction, and complexation.[15] However, a general obstacle with powdered materials used as sorbents, such as ESMs, is their separation from the treated samples. To solve this issue, the incorporation of magnetic properties into adsorbents has become the best approach.[16,17] While an eggshell membrane has been recognized as a promising biosorbent for dye removal, previous studies have mostly used it in its raw form. In a study, the untreated ESM is utilized mainly due to the electrostatic attraction,[18] while another group used the whole eggshell (with its membrane) for the removal of CR.[19] It is well reported that the membrane part works better than the shell because it is rich in amine and carboxyl groups.[20] However, the problem is that the ESM is hard to separate from water once used because it is too fine, making it inconvenient to reuse. Adding magnetic nanoparticles solves that issue, since it can just pull the adsorbent out with a magnet. The current study fills that gap by

---

Department of Chemistry, College of Science, King Faisal University, Hofuf, Eastern Province Al-Ahsa-31982, Kingdom of Saudi Arabia. E-mail: fshah@kfu.edu.sa

preparing Fe_3O_4@ESM, a magnetic bio-hybrid composite with a competent adsorption efficiency and easy recovery, thus turning waste into a sustainable sorbent. Magnetite (Fe_3O_4) nanoparticles offer an ideal solution, enabling the rapid and efficient recovery of spent adsorbents using an external magnetic field.[21] This not only simplifies the process but also enhances the reusability and economic feasibility of the material.

This work reports the rational design and synthesis of a novel, magnetic bio-hybrid adsorbent by functionalizing the fibrous protein network of the avian eggshell membrane with magnetite nanoparticles. The proposed sorbent Fe_3O_4@ESM synergistically combines its remarkable adsorption capacity due to the proteinaceous ESM with the excellent magnetic separability of magnetite nanoparticles. The study assumes that CR's negatively charged sulfonate groups have strong attraction for protonated amino groups on the ESM surface, and the porous structure along with other functional groups facilitates high-capacity uptake. This study investigates the effectiveness of the Fe_3O_4@ESM magnetic composite as a high-performance sorbent for the elimination of CR from aqueous media. The proposed sorbent was thoroughly characterized, and its adsorption performance was evaluated while following batch experiments to explore the effect of main parameters such as pH, contact time, initial dye concentration, and temperature. The adsorption kinetic, isotherm, and thermodynamic studies were also conducted to explain the fundamental adsorption mechanism. The results reveal that the Fe_3O_4@ESM composite is not only a favorably efficient and magnetically separable adsorbent but also a new sustainable tool for advanced wastewater treatment.

Materials and methods

Preparation of reagent stock solution

All chemicals used were of analytical grade and used without further purification. Iron sulfate pentahydrate ($Fe(SO_4)\cdot 5H_2O$), iron nitrate nonahydrate ($Fe(NO_3)_3\cdot 9H_2O$), ammonium hydroxide, ethanol, sodium hydroxide, and hydrochloric acid were purchased from Daejung Chemicals and Metals, South Korea. Acetic acid was obtained from AnalaR NORMAPUR, Avantor, Inc. (Radnor, PA, USA). Congo red was purchased from Thermo Fisher Scientific Inc. (Waltham, MA, USA) and used without further purification. Distilled water was used during all experimental work for solution preparation and washing purposes. An analyte stock solution (100 mg L^{-1}) was prepared by adding 1 g of CR in 1000 mL of distilled water and dissolving under continuous stirring for 2 hours. The freshly prepared solution was stored in an amber glass bottle at 4 °C to avoid the photodegradation of the dye. Working solutions of desired concentrations (50–500 mg L^{-1}) were prepared on daily basis, simply by appropriate dilution with distilled water.

Eggshell membrane separation and pretreatment

Eggshells were collected from local food shops and thoroughly washed with tap water followed by distilled water to ensure the removal of surface contaminants. These cleaned eggshells were kept submerged in distilled water for 24 hours at room temperature. This process softened the membrane and eased its detachment from the calcified shell. After soaking, the ESMs were peeled away physically from their shells with forceps. To remove the remaining deposited $CaCO_3$ for exposing functional groups on the ESM surface, the separated membranes were treated with 5% acetic acid for 24 hours. Following this acid treatment, ESMs were washed repeatedly with distilled water to achieve a neutralize pH, followed by drying in a convection oven at 60 °C for 24 hours. The dried ESMs were cut into small ∼0.5 × 0.5 cm pieces using stainless steel scissors prior to their composite synthesis.

Synthesis of Fe_3O_4 nanoparticles by a co-precipitation method

$Fe(NO_3)_3\cdot 9H_2O$ and $Fe(SO_4)\cdot 5H_2O$ in 2 : 1 molar ratio were dissolved in 200 mL distilled water at 70 °C. Under continuous stirring, 20 mL of 30% ammonia solution was added dropwise. This step changed the color of the mixture to deep black, confirming the magnetite formation. This step was proceeded for the next 30 minutes to ensure proper particle growth. The resultant suspension was cooled to room temperature. The synthesized Fe_3O_4 nanoparticles were magnetically separated and washed multiple times with distilled water and ethanol until the supernatant reached a neutral pH. The final product was dried at 80 °C in an oven until a constant mass was attained.

Synthesis of Fe_3O_4@ESM composites

The magnetic Fe_3O_4@ESM composite was prepared by immobilizing Fe_3O_4 nanoparticles onto an ESM surface. The pretreated ESM (1.0 g) and freshly synthesized Fe_3O_4 nanoparticles (0.5 g) were dispersed in 50 mL of distilled water. The pH of this mixture was adjusted to 11–12 with 0.1 M NaOH to promote electrostatic binding. The mixture was kept under continuous stirring for 24 hours at room temperature to ensure the immobilization of Fe_3O_4 nanoparticles onto the ESM surface. Finally, the magnetic Fe_3O_4@ESM composite was separated with the aid of an external magnet. The composite was thoroughly washed with distilled water to remove any unbound nanoparticles. The final Fe_3O_4@ESM composite was dried and stored until its application.

Magnetic solid-phase extraction procedure

Batch adsorption experiments were conducted to examine the effects of various parameters on the CR removal efficiency. Unless otherwise specified, each experiment was performed by adding 250 mg of Fe_3O_4@ESM to 100 mL of CR solution (100 mg L^{-1}) in 250 mL Erlenmeyer flasks. The mixtures were agitated at 150 rpm and 30 °C ± 2 °C for 60 minutes using a mechanical shaker. After agitation, the adsorbent was separated using an external neodymium magnet, and the residual CR concentration in the supernatant was analyzed using a UV-vis spectrophotometer at $\lambda_{max} = 497$ nm. All experiments were conducted in triplicate.

Optimization of experimental parameters

The experimental parameters were systematically investigated to optimize the adsorption conditions. The temperature was controlled by using a temperature-regulated shaking incubator, operating in the range of 20 °C–50 °C, while the pH was set in the range of 4–7 (adjusted with 1 M HCl/NaOH). Other parameter studies were sorbent dosage, contact time, initial dye concentration and sample volume while keeping the sorbent mass constant. A sequential multivariate optimization approach was employed. First, a Plackett–Burman design (PBD) was used to screen the five factors (pH, temperature, sorbent dosage, contact time, and sample volume) and identify the most significant parameters affecting CR removal. Subsequently, a central composite design (CCD) with response surface methodology (RSM) was applied to optimize the significant factors and investigate their interactive effects. To ensure reproducibility, all experiments were performed in triplicate. Blank experiments (without adsorbent) were conducted to confirm that dye loss due to photodegradation or container adsorption was negligible. Control experiments (without dye) were also performed to ensure that no interfering species were released from the adsorbent.

Results and discussion

Characterization of Fe_3O_4@ESM

The FTIR analysis confirmed the successful synthesis of the Fe_3O_4@ESM composite. The pristine ESM spectrum revealed key functional groups, including hydroxyl and amine (3285 cm^{-1}) and carbonyl (1636 cm^{-1}),[22] and the peaks at 1650 and 1530 cm^{-1} are associated with amine and amide groups.[23,24] The composite spectrum retained these organic peaks while displaying new, distinct Fe–O vibration bands at 590 and 837 cm^{-1}, providing unequivocal evidence for the presence of magnetite. Additionally, the second absorption band, at 900 cm^{-1}, corresponds to the bending vibration associated with the O–H bond.[25] The O–H in-plane and out-of-plane bonds appear at 1550 cm^{-1} and ~800 cm^{-1}, respectively.[26] The coexistence of these organic and inorganic signatures validates the successful integration of Fe_3O_4 nanoparticles onto the ESM matrix, confirming the formation of the magnetic composite through a firm organic–inorganic association. The FTIR spectra of ESM and Fe_3O_4@ESM are shown in Fig. 1(a and b).

As shown in Fig. 2(a and b), the dynamic light scattering (DLS) analysis confirmed the successful surface modification of the nanoparticles. Pristine Fe_3O_4 nanoparticles exhibited a hydrodynamic diameter of 396 nm, indicative of some agglomeration due to magnetic interactions. After functionalization with ESM, the composite's diameter increased to 459 nm. This 63 nm increase is attributed to the formation of a stable organic coating around the particles. The narrow size distribution for both samples indicates good dispersibility. The ESM layer provides steric stabilization, which suppresses agglomeration and enhances the colloidal stability of the suspension, a crucial factor for its performance in subsequent applications.

Zeta potential analysis revealed the colloidal stability of pristine Fe_3O_4 nanoparticles and Fe_3O_4@ESM. As presented in Fig. S1, the pristine Fe_3O_4 nanoparticles showed a zeta potential of −28.3 mV, which slightly increased to −29.0 mV in the case of the Fe_3O_4@ESM composite. Both values go above the threshold value of ±25 mV, suggesting strong electrostatic repulsion that prevents their aggregation, ensuring stable aqueous dispersions. This slight increase also suggests that the ESM coating introduced extra anionic functionalities. Furthermore, it proves an even surface charge, thus confirming that the ESM functionalization successfully modified the nanoparticles while sustaining their excellent colloidal stability for later applications.

The magnetic properties of the pristine Fe_3O_4 and Fe_3O_4@-ESM composite were examined through vibrating sample magnetometry (VSM). Pristine Fe_3O_4 nanoparticles showed strong ferrimagnetic behavior with a characteristic S-shaped hysteresis loop, which is attributed to its inverse spinel structure (Fig. S2). After its immobilization on non-magnetic ESM, the resulting Fe_3O_4@ESM composite demonstrated a decline in its saturation magnetization. Remanent magnetization

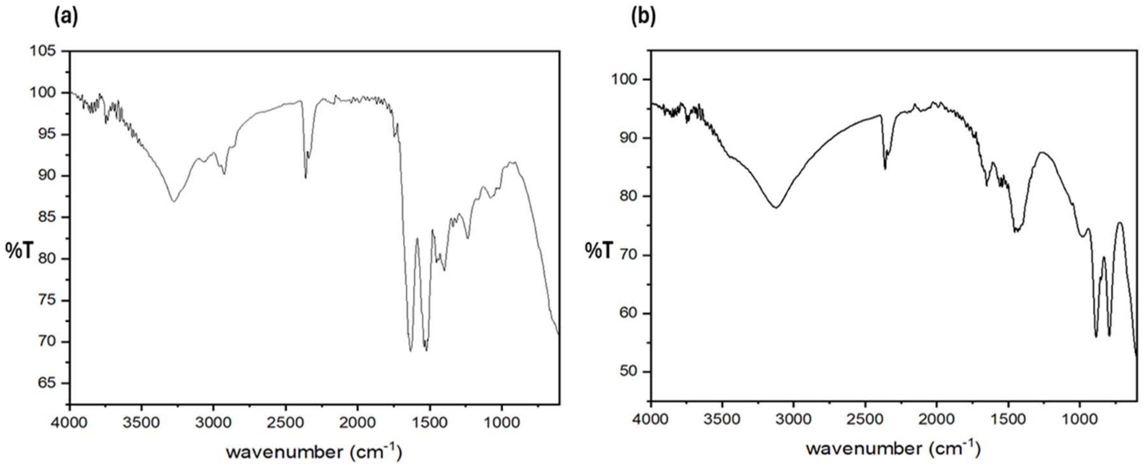

Fig. 1 FTIR spectra of (a) ESM and (b) Fe_3O_4@ESM.

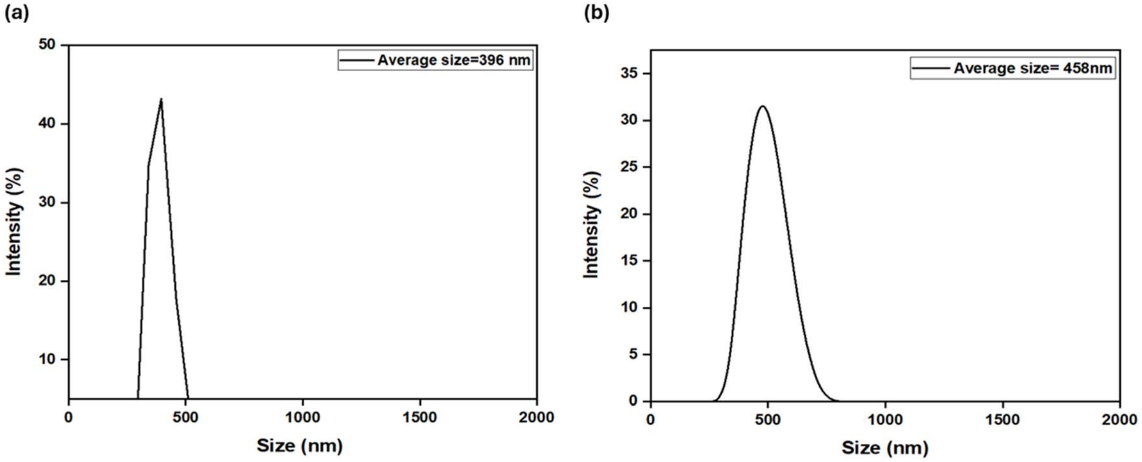

Fig. 2 Hydrodynamic sizes of (a) Fe_3O_4 nanoparticles and (b) Fe_3O_4@ESM.

Table 1 Calculated VSM parameters of Fe_3O_4 and Fe_3O_4@ESM

Parameters	Fe_3O_4	Fe_3O_4@ESM
Magnetization at 7000 (emu g^{-1})	22	1.82
Remanent magnetization (emu g^{-1})	0.61	0.03
Coercivity (H_c)	13	12.5

decreased from 0.61 to 0.03 emu g^{-1} for Fe_3O_4@ESM (as shown in Table 1). This is justified due to the dilution effect of the organic coating (of non-magnetic ESM) and the introduction of a magnetically dead layer on the Fe_3O_4 nanoparticle surface. Significantly, the composite retained sufficient ferrimagnetic properties, assisting its effective separation through external magnetic field. This crucial property ensures its practical utilization in applications such as environmental remediation and catalysis.

Scanning electron microscopy (SEM) images revealed the structural integration of the composite (Fig. 3a and b). The pristine ESM demonstrated a characteristic 3D porous network of interlinked protein fibers. This framework provides a high surface area for nanoparticle binding. The Fe_3O_4@ESM composite images confirmed the successful immobilization of Fe_3O_4 nanoparticles onto this fibrous matrix. An intrinsic porous framework of ESMs was maintained, which allowed the efficient mass transfer. The homogeneous layer of Fe_3O_4 nanoparticles combines the structural advantages of the ESM with magnetic functionality, resulting in a hybrid material which is suitable for catalysis and environmental applications.

The pH_{pzc} value of the Fe_3O_4@ESM composite was measured to be 5.9, lower than that of Fe_3O_4 nanoparticles (Fig. S3). This shift proves the successful coating of Fe_3O_4 nanoparticles over the ESM matrix, carrying carboxylic groups on the surface due to its proteinaceous structure. Fig. 4 indicates the results obtained from the Brunauer–Emmett–Teller (BET) surface area analysis. The specific surface area was estimated using the BET equation, while the BJH method was used for pore size distribution. The results from nitrogen physisorption studies revealed that the Fe_3O_4@ESM composite has a BET surface area of 9.62 m^2 g^{-1} with a total pore volume of 0.131 cm^3 g^{-1}. The pore size distribution signifies a mesoporous configuration with a predominant pore diameter of 3.8 nm. The type IV isotherm with an H3-type hysteresis loop indicates the existence of slit-shaped pores, which are the characteristic of layered materials. This mesoporous network and moderate surface area enable the diffusion and adsorption of large dye molecules like CR.

Optimization through response surface methodology

A multivariate optimization strategy was followed to determine the optimum conditions for CR adsorption through the Fe_3O_4@ESM composite. Five main parameters including pH, temperature, sorbent dosage, contact time and sample volume

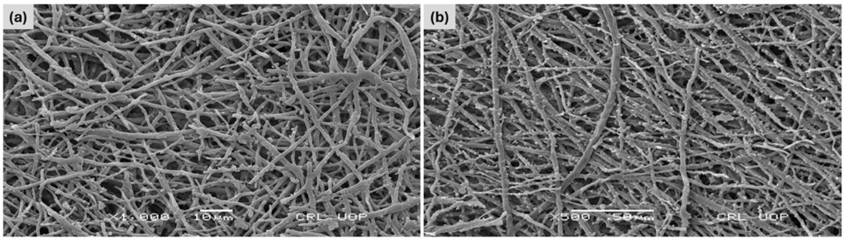

Fig. 3 SEM images of (a) Fe_3O_4 nanoparticles and (b) Fe_3O_4@ESM.

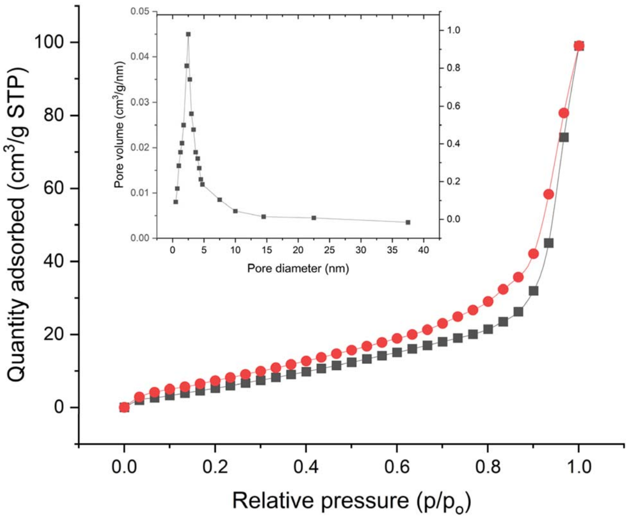

Fig. 4 N_2 physisorption analysis of the Fe_3O_4@ESM composite: adsorption–desorption isotherms and the corresponding Barrett–Joyner–Halenda (BJH) pore size distribution plot.

were investigated. All these parameters and their levels are shown in Table 2. The optimization utilized a subsequent strategy using Minitab 17.1, starting with factor screening *via* PBD followed by detailed analysis through CCD and RSM.

Factor screening and significance analysis

Initial screening *via* the Plackett–Burman design successfully identified the most significant parameters. Table 3 displays the complete PBD with 24 experiments and the observed responses. The Pareto chart analysis shown in Fig. 5 revealed that the pH (A), sorbent dosage (C), and contact time (D) have the most significant effects on CR adsorption ($p < 0.05$). The significant effect of pH supports the fundamental chemistry of CR adsorption.[27] CR, an anionic dye, demonstrates enhanced adsorption under acidic conditions where the Fe_3O_4@ESM surface becomes protonated, acquiring a positive charge that facilitates strong electrostatic attraction with the dye sulfonate groups.[28] The Fe_3O_4@ESM composite possesses amphoteric surface functional groups. The ESM biopolymer is rich in –COOH (from amino acids like aspartic and glutamic acid) and –NH_2 (from lysine, *etc.*) groups, while the magnetite surface has Fe–OH sites.[29] In acidic media where the pH is below the point of zero charge (PZC) of the composite, these groups become protonated, resulting in a positively charged surface due to >Fe–OH_2^+ and –NH_3^+. Congo red is an anionic azo dye with sulfonate groups (–SO_3^-) that are fully deprotonated and remain negatively charged across a wide pH range. At the optimum pH of 5.7, the composite surface is protonated enough (because of –NH_3^+ and Fe–OH_2^+ groups) to carry an overall positive charge, while the CR molecules remain negatively charged (due to the presence of –SO_3^- groups). This creates strong electrostatic interaction, which is the main driving force for adsorption.

Table 2 Factors and levels used in the factorial design

Factors	ID	Unit	Lower⁻	High⁺	Optimum
pH	A	—	4	7	5.7
Temperature	B	°C	20	50	30
Sorbent dosage	C	mg	100	300	250
Contact time	D	min	10	180	60
Sample volume	E	mL	20	50	40[a]

[a] Insignificant factors with convenient values.

Table 3 Plackett–Burman design and the % removal efficiency

S. no.	A	B	C	D	E	% Removal
1	—	—	—	+	—	97.3 ± 3.3
2	+	—	+	—	—	91.6 ± 3.1
3	+	—	—	+	+	99.1 ± 2.1
4	+	+	—	—	—	76.5 ± 2.7
5	+	+	+	—	—	45.3 ± 1.4
6	+	—	+	+	+	45.8 ± 1.9
7	—	+	+	—	+	48.1 ± 2.2
8	+	—	+	—	+	43.2 ± 1.7
9	+	—	—	+	+	44.3 ± 1.9
10	—	—	+	+	—	45.7 ± 2.3
11	—	—	+	+	—	44.4 ± 1.9
12	—	—	—	—	+	42.9 ± 1.6
13	+	—	—	—	—	44.9 ± 1.8
14	+	+	+	+	—	44.2 ± 1.4
15	—	+	—	+	—	41.5 ± 1.1
16	—	+	—	—	+	42.1 ± 1.2
17	—	+	+	—	—	44.3 ± 1.9
18	—	—	+	—	+	43.3 ± 1.6
19	—	—	—	—	—	45.4 ± 2.2
20	+	+	—	+	—	42.2 ± 1.4
21	+	+	+	+	+	44.6 ± 1.8
22	+	+	—	—	+	47.3 ± 2.7
23	—	+	+	+	+	42.4 ± 1.4
24	—	+	—	+	+	46.5 ± 2.4

At higher pH (>7), the surface deprotonates (>Fe–O^- and –COO^-), leading to a negatively charged surface followed by electrostatic repulsion between the sorbent surface and anionic dye, significantly lowering the dye uptake.[30]

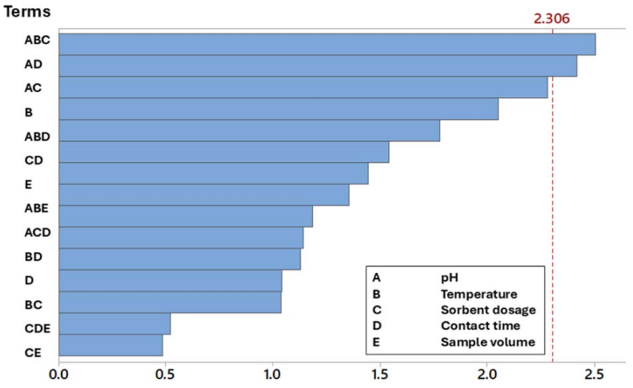

Fig. 5 Pareto chart of the factorial tentative design for the study of parameters.

The presence of abundant hydroxyl (–OH), amine (–NH_2), and amide (–CONH–) groups on the ESM surface provides multiple hydrogen bond donor and acceptor sites.[31] These functional groups can form hydrogen bonds with the nitrogen atoms of the azo bonds (–N═N–), oxygen atoms of the sulfonate groups (–SO_3^-) and the aromatic ring systems of the CR molecule. This is consistent with previous reports on dye adsorption onto proteinaceous materials. Saratale *et al.* similarly attributed reactive dye adsorption onto ESM to hydrogen bonding interactions, observing shifts in O–H/N–H stretching bands after adsorption.[18] Abdel-Khalek *et al.* also reported hydrogen bonding contributions in CR adsorption onto an eggshell matrix.[19] The ESM protein matrix contains aromatic amino acid residues (*e.g.*, phenylalanine, tyrosine, and tryptophan) that possess aromatic ring structures. CR is a highly aromatic molecule containing naphthalene and biphenyl structures with conjugated π-electron systems. These aromatic moieties can engage in π–π stacking interactions between the electron-rich aromatic rings of ESM proteins and the aromatic rings of CR.

Furthermore, the chelation between Fe sites and dye groups was not identified as a dominant mechanism, as CR does not possess strong metal-chelating functional groups (*e.g.*, –COOH and –OH in ortho position to azo groups) that would typically form stable Fe-dye complexes.

Temperature (B) exhibited a moderate but significant effect, with an optimal value at 30 °C. The increase in temperature from 20 °C to 30 °C increases the kinetic energy of the CR molecules, leading to an increase in the diffusion rate of dye molecules from the bulk solution to the adsorbent surface and within its pores. This increase in temperature results in faster adsorption kinetics and a higher initial rate of removal. Physical adsorption processes, including electrostatic interactions, are typically exothermic. Desorption occurs as the thermal energy increases beyond the optimum temperature (*e.g.*, at 50 °C). The CR molecules gain sufficient kinetic energy to overcome the attractive forces binding them to the surface, and the overall adsorption capacity is decreased.[32] Additionally, the increase in temperature can cause some swelling or structural alterations in the ESM polymeric framework, possibly blocking pores or reducing active sites.

The sample volume (*E*) established the least significance within the tested range, suggesting the robustness of the adsorption process concerning solution volume when the CR concentration remains unchanged.

Response surface analysis and parameter interactions

The central composite design for the significant factors and their % removal efficiency are presented in Table 4. The CCD-based response surface plots (Fig. 6a–d) provided detailed insights into the interactive effects between the critical parameters. The interaction between the pH and the sorbent dosage revealed that the highest adsorption yields were achieved at lower pH levels (4–6) combined with higher sorbent doses (250–300 mg). This synergy occurs because the protonated surface sites at low pH are maximally utilized when enough adsorbent is present.

Table 4 Central composite design for the set of factors A, B, C and D

S. no.	A	B	C	D	% Removal
1	${}_{a}A$	${}_{a}B$	${}_{a}C$	${}_{a}D$	82.5 ± 3.5
2	—	—	—	—	48.3 ± 2.9
3	+	—	—	—	48.2 ± 2.4
4	—	+	—	—	49.1 ± 3.1
5	+	+	—	—	35.3 ± 2.5
6	—	—	+	—	72.4 ± 3.4
7	+	—	+	—	46.3 ± 2.8
8	—	+	+	—	28.2 ± 2.4
9	+	+	+	—	26.1 ± 2.1
10	—	—	—	+	8.4 ± 1.6
11	+	—	—	+	12.3 ± 1.9
12	—	+	—	+	9.2 ± 1.8
13	+	+	—	+	10.5 ± 2.2
14	—	—	+	+	4.3 ± 0.1
15	+	—	+	+	5.4 ± 1.1
16	—	+	+	+	15.4 ± 2.1
17	${}^{-}{}_{a}A$	${}_{a}B$	${}_{a}C$	${}_{a}D$	17.2 ± 2.3
18	$+_{a}A$	${}_{a}B$	${}_{a}C$	${}_{a}D$	18.1 ± 2.8
19	${}_{a}A$	$+_{a}B$	${}_{a}C$	${}_{a}D$	15.3 ± 2.4
20	${}_{a}A$	${}^{-}{}_{a}B$	${}_{a}C$	${}_{a}D$	17.1 ± 2.9
21	${}_{a}A$	${}_{a}B$	${}^{-}{}_{a}C$	${}_{a}D$	18.4 ± 2.3
22	${}_{a}A$	${}_{a}B$	$+_{a}C$	${}_{a}D$	9.1 ± 1.8
23	${}_{a}A$	${}_{a}B$	${}_{a}C$	${}^{-}{}_{a}D$	5.3 ± 1.3
24	${}_{a}A$	${}_{a}B$	${}_{a}C$	$+_{a}D$	15.5 ± 2.6

The positive correlation between the adsorbent dosage and removal efficiency is due to the increase in available surface area and adsorption sites.[33] The interaction between sorbent dosage and contact time indicated that with higher adsorbent loads (>250 mg), the system reached equilibrium more rapidly (within 60 minutes). Increasing the dose from 100 to 250 mg provides a greater number of active binding sites for a fixed amount of CR, leading to a higher percentage of dye removal. This is attributed to the increased availability of surface sites, reducing the diffusion path length and time required for CR molecules to encounter binding sites. Beyond a certain point, the removal efficiency of CR decreases. This is because, at very high doses (*e.g.*, 300 mg), the particles may aggregate due to overcrowding, which reduces the total effective surface area and can hinder diffusion.[34] The adsorption capacity (milligrams of dye adsorbed per gram of sorbent) often decreases with the increasing dose, as the sites remain unsaturated.

The 60 minutes optimum represents the time required to reach a dynamic equilibrium between adsorption and desorption. The initial stage of contact is characterized by a very fast adsorption rate due to the high concentration gradient and the abundance of vacant surface sites. As time progresses, the vacant sites are filled, the concentration gradient decreases, and the repulsive forces between the dye molecules already adsorbed and those in the solution increase. By 60 minutes, the system reaches a state where the rate of adsorption equals the rate of desorption, and no significant further uptake occurs. Longer times are operationally inefficient.

For a fixed mass of sorbent and initial dye concentration, the sample volume influences the concentration gradient, which is the driving force for mass transfer. At a very low sample volume

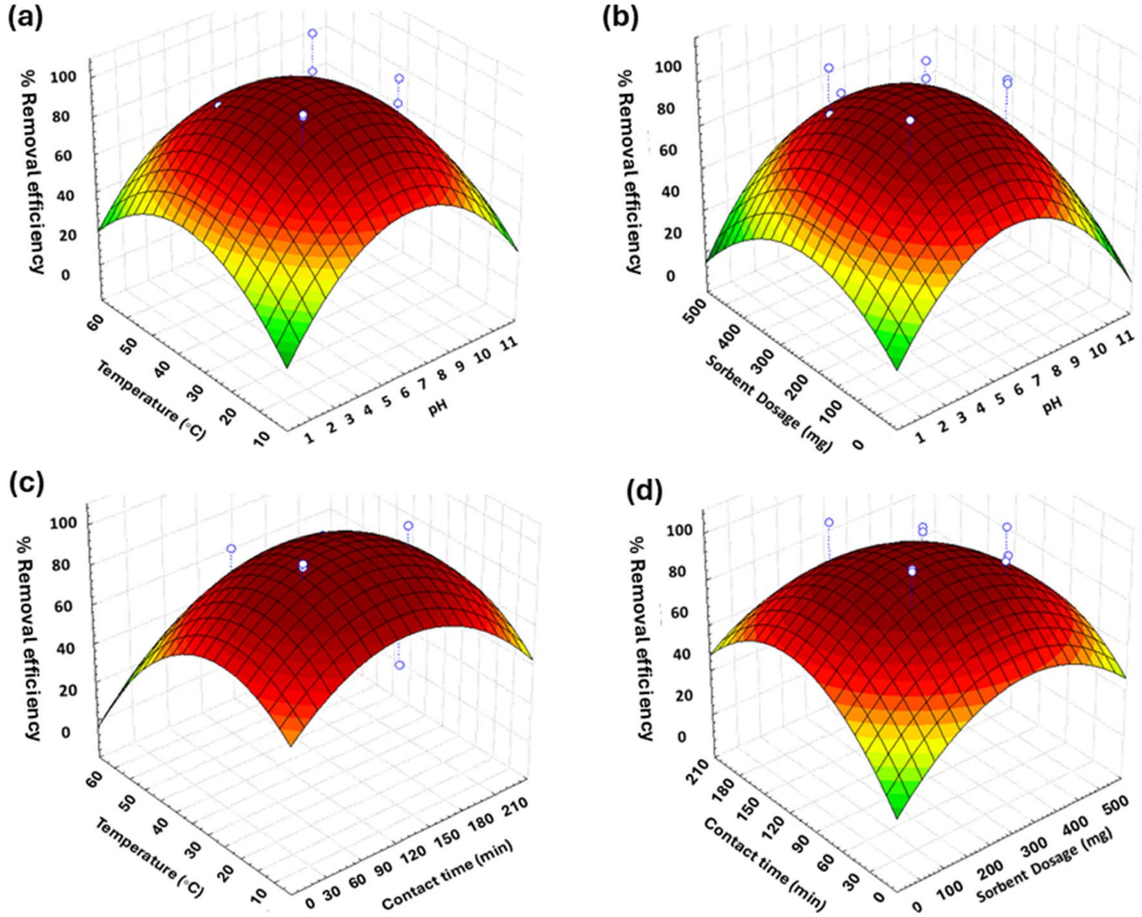

Fig. 6 3D response surface plot against (a) pH and temperature, (b) pH and sorbent dosage, (c) contact time and temperature, and (d) sorbent dosage and contact time.

(*e.g.*, 20 mL), the absolute number of dye molecules is low, and while the removal percentage is high, the process is not resource-efficient for treating larger volumes. At a very high volume (50 mL), the ratio of sorbent to solute is less favorable, and the distance that dye molecules must diffuse to reach a site can increase, potentially slightly reducing the efficiency. The 40 mL optimum represents a volume where the sorbent's capacity is utilized effectively without introducing significant mass transfer limitations, ensuring a high driving force for adsorption while maintaining practical applicability.

The model's predictive capability was validated through confirmation experiments under the predicted optimum conditions (pH: 5.7, temperature: 30 °C, sorbent: 250 mg, contact time: 60 min, sample volume: 40 mL). The strong agreement between the experimental results and model predictions ($R^2 > 0.95$) confirms the reliability and accuracy of the developed quadratic models. The optimization process successfully identified a set of conditions that maximize CR removal while ensuring the efficient use of the Fe_3O_4@ESM composite, providing a solid foundation for potential scale-up and application in wastewater treatment scenarios.

Adsorption studies

The adsorption capacity of the surface-modified sorbent was evaluated by introducing 250 mg of the material into 100 mL of a CR solution with an initial concentration (C_i) of 100 mg L^{-1}. This mixture was shaken in a 100 mL Erlenmeyer flask at 300 rpm and 30 °C for 24 hours. Following agitation, the aqueous phase was separated, and the residual CR concentration at equilibrium (C_e) was determined using a UV/vis spectrophotometer. The adsorption capacity (q) was subsequently calculated according to eqn (1) as follows:

$$q = V(C_i - C_e)/W. \tag{1}$$

In these equations, V is the volume of the solution (mL) and W is the mass of the Fe_3O_4@ESM sorbent (mg).

To investigate the adsorption equilibrium, the Langmuir, Freundlich and Temkin isotherm models were applied (Fig. S4a–c). The Langmuir model (eqn (2)), which describes the monolayer adsorption on a homogeneous surface, was analyzed using its linearized form given in eqn (3) as follows:

$$q_e = \frac{q_{\max} K_L C_e}{1 + K_L C_e}, \tag{2}$$

$$\frac{1}{q_\mathrm{e}} = \frac{1}{K_\mathrm{L} q_\mathrm{max}} \times \frac{1}{C_\mathrm{e}} + \frac{1}{q_\mathrm{max}}. \tag{3}$$

In this model, q_max is the maximum adsorption capacity (mg g^{-1}), and K_L (L mg^{-1}) is the Langmuir constant, which reflects the binding affinity between CR and the sorbent. The favorability of the adsorption process was assessed using the dimensionless separation factor (R_L), calculated with eqn (4). Based on the R_L value, adsorption can be classified as irreversible ($R_\mathrm{L} = 0$), favorable ($0 < R_\mathrm{L} < 1$), linear ($R_\mathrm{L} = 1$), or unfavorable ($R_\mathrm{L} > 1$) as follows:[35]

$$R_\mathrm{L} = \frac{1}{1 + C_\mathrm{i} \times K_\mathrm{L}}. \tag{4}$$

The Freundlich isotherm model (eqn (5)) describes adsorption on heterogeneous surfaces. Its linearized form is given by eqn (6) as follows:

$$q_\mathrm{e} = K_\mathrm{f} C_\mathrm{e}^{\frac{1}{2}}, \tag{5}$$

$$\log q_\mathrm{e} = \log K_\mathrm{f} + \frac{1}{n} \log C_\mathrm{e}. \tag{6}$$

In the Freundlich model, K_f is the Freundlich constant, representing the adsorption capacity, and $1/n$ indicates the adsorption intensity. A value of $1/n$ between 0.1 and 0.5 suggests favorable adsorption, whereas a value exceeding 2 suggests an unfavorable process.[36]

The Temkin isotherm model was applied to the equilibrium data, showing a good linear relationship with $R^2 = 0.976$. The Temkin constants were determined as $K_\mathrm{t} = 0.298$ L g^{-1} and $B = 8.092$. The K_t value indicates moderate binding affinity between the CR dye and the Fe_3O_4@ESM adsorbent. The model is given by the following equation:

$$q_\mathrm{e} = \frac{RT}{b} \ln\left(K_\mathrm{t} C_\mathrm{e}\right). \tag{7}$$

The linear form of the model can be expressed as follows:

$$q_\mathrm{e} = B_\mathrm{T} \ln K_\mathrm{t} + B_\mathrm{T} \ln C_\mathrm{e}, \tag{8}$$

$$q_\mathrm{e} = \frac{RT}{b_\mathrm{t}} \ln K_\mathrm{t} + \left(RT/b_\mathrm{t}\right), \tag{9}$$

where the constant B_T is defined as follows:

$$B_\mathrm{T} = RT/b_\mathrm{t} \tag{10}$$

The equilibrium data were further analyzed using the Temkin isotherm model, which yielded an excellent fit with a high regression coefficient ($R^2 = 0.992$). The positive value of b_t confirms the exothermic nature of the adsorption process. Its low magnitude suggests that physisorption is the primary mechanism, likely involving electrostatic interactions.[37] The significant value of the constant B_T indicates a linear decrease in the heat of adsorption with the increasing surface coverage, which is attributed to the repulsive interactions between the adsorbed CR molecules on the homogeneous surface of the Fe_3O_4@ESM composite. The equilibrium binding constant (K_t) value of 0.494 L g^{-1} indicates a moderate affinity between the dye and the sorbent.[38] All these results are shown in Table 5. By integrating the insights from the Langmuir, Freundlich and Temkin models, a comprehensive understanding of the adsorption behavior and surface interactions between CR and the Fe_3O_4@ESM sorbent was achieved.

Table 5 Isotherm and kinetic parameters for the adsorption of CR by Fe_3O_4@ESM

Isotherm parameters

Type of isotherm	Parameter	
Langmuir	q_max (mg g^{-1})	45.04
	K_L (L mg^{-1})	0.024
	R_L	0.451
	R^2	0.999
Freundlich	K_f	2.47
	$1/n$	0.519
	R^2	0.920
Temkin	b_T	303.95
	B_t	8.288
	K_t (L g^{-1})	0.494
	R^2	0.992

Kinetic parameters

Order of reaction	Parameter	
Pseudo-first order	$q_\mathrm{e,\,cal}$ (mg g^{-1})	1.679
	K_1 (min^{-1})	-7.70×10^{-4}
	R^2	0.567
Pseudo-second order	$q_\mathrm{e,\,cal}$ (mg g^{-1})	34.96
	K_2 (g mg^{-1} min^{-1})	0.066
	R^2	0.999

Kinetic study

To understand the adsorption rate, the kinetics of CR on Fe_3O_4@ESM was evaluated by fitting the data to pseudo-first-order and pseudo-second-order kinetic models (Fig. S4d and e). The linear form of the pseudo-first-order model is expressed as eqn (7):

$$\ln\left(q_\mathrm{e} - q_t\right) = \ln q_\mathrm{e} - K_1 t. \tag{11}$$

where q_t denotes the adsorption capacity (mg g^{-1}) at time t, q_e is the equilibrium adsorption capacity (mg g^{-1}), and K_1 (min^{-1}) is the equilibrium rate constant.

The pseudo-second-order kinetic model (eqn (12)) provides an alternative description, where K_2 (g mg^{-1} min^{-1}) is the model's rate constant as follows:

$$\frac{t}{q_\mathrm{e}} = \frac{1}{K_2 {q_\mathrm{e}}^2} + \frac{1}{q_\mathrm{e}}. \tag{12}$$

Table 5 shows the results of kinetic parameters for the adsorption of CR by Fe_3O_4@ESM. Pseudo-second order was

Table 6 Comparison of the adsorption capacity of the proposed adsorbent with those reported

Adsorbent	Adsorption capacity (mg g^{-1})	Reference
Untreated bottom ash	24.36	40
Fly ash	22.12	41
Bagasse fly ash	11.88	42
Calcium rich fly ash	9.41	43
Zeolite	9.23	44
Zeolite/algae composite	12.25	
$ZnCr_2O_4$ oxide	44.04	45
$MgCr_2O_4$ oxide	43.59	
$CoCr_2O_4$ oxide	28.72	
Coconut fiber-based activated carbon	22.10	46
Kenaf-based activated carbon	14.20	47
Mango leaves	21.28	48
Litchi seed	20.49	49
Apricot stone	32.68	50
Fe_3O_4@ESM	45.04	Current study

selected as the best-fitting kinetic model based on the regression coefficient (R^2).

Among the ESM-based adsorbents, our Fe_3O_4@ESM composite (45.04 mg g^{-1}) performs similarly to or slightly better than the other ESM-based materials reported earlier, like the whole eggshell matrix (49.5 mg g^{-1}),[19] eggshell biocomposite beads (46.9 mg g^{-1})[39] and plain ESM by itself (13.1 mg g^{-1}).[20] However, in a study, 191.5 mg g^{-1} adsorption capacity has been reported for a different analyte (dye) using the ESM alone, but that material cannot be separated easily, involving centrifugation or filtration each time.[18] In contrast, the proposed Fe_3O_4@ESM composite achieves a decent 45.04 mg g^{-1} for Congo red and can be separated magnetically in seconds, which is a real operational advantage. The magnetic addition basically turns a simple biosorbent into something practical for wastewater treatment. The adsorption capacity of Fe_3O_4@ESM was found to be competitive with other sorbents (Table 6), demonstrating the method's reliability and potential for CR removal.

The thermodynamic studies revealed negative values for both Gibbs free energy and enthalpy, along with a positive entropy change (Table 7). These results indicate that this adsorption is a spontaneous, exothermic, and entropy-driven process. The negative ΔH^0 value proves strong exothermic interactions between the CR molecules and the sorbent surface, suggesting that chemisorption is the adsorption mechanism.[51,52] Similarly, the positive value for ΔS^0 reveals that the adsorption is enhanced by a solvent displacement effect. This means that the structured water molecules from the sorbent surface are released into the bulk solution, which increases the randomness of the overall system. The favorable values for enthalpy and entropy changes indicate a highly spontaneous adsorption process, highlighting the effectiveness of Fe_3O_4@ESM for dye removal applications.

Table 7 Thermodynamic parameters for the adsorption of CR onto Fe_3O_4@ESM

Temperature (K)	ΔG^0 (kJ mol^{-1})	ΔH^0 (kJ mol^{-1})	ΔS^0 (J mol^{-1} K^{-1})	R^2
303	−16.02	−5.68	34.12	0.999
313	−16.37			
323	−16.71			

Validation of SPE

The developed method was validated to determine its efficiency for practical applications. This study was carried out through a standard addition method, where aliquots of CR were added into real wastewater samples. Following the solid-phase magnetic extraction under optimal conditions, the samples were analyzed by spectrophotometry to quantify the CR concentration. This procedure decreased interference from the sample matrix, resulting in excellent recoveries. As shown by the recovery data in Table S1, the standard addition methodology confirmed the robustness and accuracy of the developed SPE procedure.

Reusability of Fe_3O_4@ESM

The reusability of Fe_3O_4@ESM was investigated by conducting five consecutive adsorption–desorption cycles under optimum

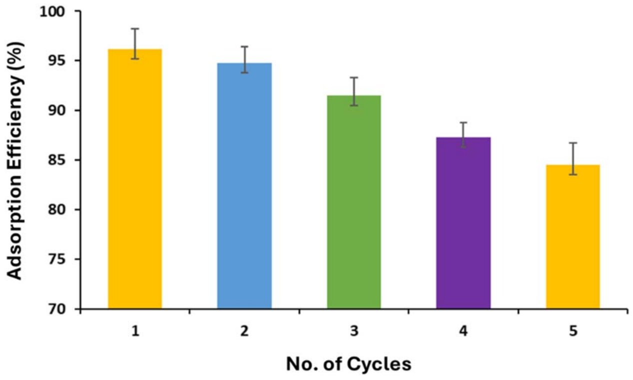

Fig. 7 Adsorption efficiency of Fe_3O_4@ESM over five consecutive cycles (n = 3).

conditions. After each run, the sorbent was taken out with an external magnetic field, desorbed with 0.1 M NaOH, washed with distilled water and reused.

The adsorption efficiency reduced steadily from 96.2% in the first cycle to 84.5% in the last cycle (Fig. 7). The slight drop in adsorption efficiency could be attributed to some active sites being permanently occupied by strongly bound CR molecules, leading to minor sorbent loss. Still, >84% efficiency after five runs demonstrates that Fe_3O_4@ESM possesses good reusability, supporting its potential for practical application.

Conclusion

This study successfully confirms Fe_3O_4@ESM as a highly effective and environmentally feasible adsorbent for the removal of CR from wastewater. Its excellent adsorption efficiency is attributed to its mesoporous structure and abundance of surface functionalities. The incorporated magnetic property enables facile separation, offering practical advantage over conventional non-magnetic biosorbents. There are also certain limitations in the current study. This study was conducted on synthetic dye solutions instead of real industrial wastewater, thus not fully representing the complexity of real samples. Moreover, long-term stability and continuous flow operation were not assessed, and the sorbent separation remains labor intensive for large-scale production. Future research should focus on performance assessment with real industrial wastewater, development of continuous flow systems and optimizing membrane separation for bulk production. Additionally, long-term stability and life cycle assessments should be conducted to investigate its application for other emerging contaminants. Addressing these aspects will further advance this sustainable adsorbent toward practical applications.

Conflicts of interest

The author declares no conflicts of interest.

Data availability

All the data produced and/or analyzed in the course of this study are presented within this manuscript and its accompanying supplementary information (SI). Supplementary information is available. See DOI: https://doi.org/10.1039/d6ra01484d.

Acknowledgements

This work was supported by the Deanship of Scientific Research, Vice Presidency for Graduate Studies and Scientific Research, King Faisal University, Saudi Arabia [Grant No. KFU261517].

References

1 T. Sarwar and S. Khan, in *Textile Wastewater Treatment: Sustainable Bio-Nano Materials and Macromolecules*, Springer, 2022, Vol 1, pp. 1–28.
2 S. Jan, A. K. Mishra, M. A. Bhat, M. A. Bhat and A. T. Jan, *Environ. Sci. Pollut. Res.*, 2023, **30**, 113242–113279.
3 F. Eltaboni, N. Bader, R. El-Kailany, N. Elsharif and A. J. Ahmida, *J. Chem. Rev.*, 2022, **4**, 313–330.
4 H. Alzain, V. Kalimugogo, K. Hussein and M. Karkadan, *Int. J. Res. Rev.*, 2023, **10**, 673–689.
5 R. Saini and K. Choudhary, in *Hazardous Chemicals*, Elsevier, 2025, pp. 469–481.
6 R. R. M. Khan, H. Qamar, A. Hameed, A. u. Rehman, M. Pervaiz, Z. Saeed, A. Adnan and A. R. Ch, *Water Air Soil Pollut.*, 2022, **233**, 468.
7 Y. Patil, S. Attarde, R. Dhake, U. Fegade and A. N. M. Alaghaz, *Int. J. Chem. Kinet.*, 2023, **55**, 579–605.
8 M.-N. Georgaki, M. Charalambous, N. Kazakis, M. A. Talias, C. Georgakis, T. Papamitsou and C. Mytiglaki, *Environ.*, 2023, **10**, 33.
9 S. I. Siddiqui, E. S. Allehyani, S. A. Al-Harbi, Z. Hasan, M. A. Abomuti, H. K. Rajor and S. Oh, *Processes*, 2023, **11**, 807.
10 R. Rashid, I. Shafiq, P. Akhter, M. J. Iqbal and M. Hussain, *Environ. Sci. Pollut. Res.*, 2021, **28**, 9050–9066.
11 M. S. Akhtar, S. Ali and W. Zaman, *Molecules*, 2024, **29**, 4317.
12 Z. Seikh, M. A. Mallick, A. S. Gazi and M. J. Sekh, *J. Inst. Eng. (India): D*, 2025, 1–15.
13 S. Takyar, *Masters thesis*, University of Saskatchewan, 2025, Online, available: https://hdl.handle.net/10388/17213.
14 M. Baláž, *Acta Biomater.*, 2014, **10**, 3827–3843.
15 J. Badillo-Camacho, E. Orozco-Guareno, G. G. Carbajal-Arizaga, R. Manríquez-Gonzalez, I. D. Barcelo-Quintal and S. Gomez, *Adsorpt. Sci. Technol.*, 2020, **38**, 413–434.
16 D. S. Dlamini, J. M. Tesha, G. D. Vilakati, B. B. Mamba, A. K. Mishra, J. M. Thwala and J. Li, *J. Clean. Prod.*, 2020, **277**, 123497.
17 J. Li, B. Jiang, Y. Liu, C. Qiu, J. Hu, G. Qian, W. Guo and H. H. Ngo, *J. Clean. Prod.*, 2017, **158**, 51–58.
18 R. G. Saratale, Q. Sun, V. S. Munagapati, G. D. Saratale, J. Park and D.-S. Kim, *Chemosphere*, 2021, **281**, 130777.
19 M. Abdel-Khalek, M. A. Rahman and A. Francis, *J. Environ. Chem. Eng.*, 2017, **5**, 319–327.
20 N. Pramanpol and N. Nitayapat, *Agric. Nat. Resour.*, 2006, **40**, 192–197.
21 N. A. I. Muddin, M. M. Badsha, M. A. Arafath, Z. M. A. Merican and M. S. Hossain, *Desalin. Water Treat.*, 2024, **319**, 100449.
22 M. S. Tizo, L. A. V. Blanco, A. C. Q. Cagas, B. R. B. D. Cruz, J. C. Encoy, J. V. Gunting, R. O. Arazo and V. I. F. Mabayo, *Sustain. Environ. Res.*, 2018, **28**, 326–332.
23 O. Bayraktar, C. M. Galanakis, T. M. Aldawoud, S. A. Ibrahim, M. D. Köse and M. E. Uslu, *Foods*, 2021, **10**, 806.
24 W. Tsai, J. Yang, C. Lai, Y. Cheng, C. Lin and C. Yeh, *Bioresour. Technol.*, 2006, **97**, 488–493.
25 J. A. Lopez, F. González, F. A. Bonilla, G. Zambrano and M. E. Gómez, *Rev. Metal.*, 2010, **30**, 60–66.
26 L. Zhang, R. He and H.-C. Gu, *Appl. Surf. Sci.*, 2006, **253**, 2611–2617.

27 Y. Bai, W. Huang, J. Liu, K. Hu, H. Zheng and X. Shen, *Langmuir*, 2025, **41**, 22129–22151.

28 G. Zemanek, A. Jagusiak, K. Chłopaś, B. Piekarska and B. Stopa, *Bio-Algorithms Med-Syst.*, 2017, **13**, 69–78.

29 S. B. Rønning, R. S. Berg, V. Høst, E. Veiseth-Kent, C. R. Wilhelmsen, E. Haugen, H.-P. Suso, P. Barham, R. Schmidt and M. E. Pedersen, *Int. J. Mol. Sci.*, 2020, **21**, 8130.

30 J. Bandara, J. Mielczarski and J. Kiwi, *Langmuir*, 1999, **15**, 7670–7679.

31 A. Arami-Niya, W. M. A. W. Daud, F. S. Mjalli, F. Abnisa and M. S. Shafeeyan, *Chem. Eng. Res. Des.*, 2012, **90**, 776–784.

32 Y. Hu, T. Guo, X. Ye, Q. Li, M. Guo, H. Liu and Z. Wu, *Chem. Eng. J.*, 2013, **228**, 392–397.

33 P. Mondal, C. Majumder and B. Mohanty, *J. Hazard. Mater.*, 2008, **150**, 695–702.

34 M. Pettinato, S. Chakraborty, H. A. Arafat and V. Calabro, *Ecotoxicol. Environ. Saf.*, 2015, **121**, 57–62.

35 O. G. Okpara, O. M. Ogbeide, O. C. Ike, K. C. Menechukwu and E. C. Ejike, *Toxin Rev.*, 2021, **40**, 901–914.

36 R.-L. Tseng and F.-C. Wu, *J. Hazard. Mater.*, 2008, **155**, 277–287.

37 M. A. Alsharif, in *Adsorption-Fundamental Mechanisms and Applications*, IntechOpen, 2025.

38 H. N. Tran, *Adsorpt. Sci. Technol.*, 2022, **2022**, 5553212.

39 M. Elkady, A. M. Ibrahim and M. Abd El-Latif, *Desalination*, 2011, **278**, 412–423.

40 S. Saleh, H. Maarof, S. Rahim and N. Nasuha, *J. Appl. Sci.*, 2012, **12**(11), 1181–1185.

41 M. Harja, G. Buema and D. Bucur, *Sci. Rep.*, 2022, **12**, 6087.

42 I. D. Mall, V. C. Srivastava, N. K. Agarwal and I. M. Mishra, *Chemosphere*, 2005, **61**, 492–501.

43 B. J. Acemioğlu, *iScience*, 2004, **274**, 371–379.

44 A. R. Dryaz, M. Shaban, H. AlMohamadi, K. A. A. Al-Ola, A. Hamd, N. Soliman and S. A. Ahmed, *Sci. Rep.*, 2021, **11**, 21058.

45 H. Gao, S. Wang, L. Fang, G. Sun, X. Chen, S. Tang, H. Yang, G. Sun and D. Li, *Mater. Today Chem.*, 2021, **22**, 100593.

46 L. Zhang, L.-y. Tu, Y. Liang, Q. Chen, Z.-s. Li, C.-h. Li, Z.-h. Wang and W. Li, *RSC Adv.*, 2018, **8**, 42280–42291.

47 S. Mandal, J. Calderon, S. B. Marpu, M. A. Omary and S. Q. Shi, *J. Contam. Hydrol.*, 2021, **243**, 103869.

48 O. A. Adelaja, A. C. Bankole, M. E. Oladipo and D. B. Lene, *Int. J. Energy Water Resour.*, 2019, **3**, 1–12.

49 J. N. Edokpayi and E. Makete, *Phys. Chem. Earth (Pt A B,C)*, 2021, **123**, 103007.

50 M. Abbas and M. Trari, *Process Saf. Environ. Prot.*, 2015, **98**, 424–436.

51 S. Żółtowska-Aksamitowska, P. Bartczak, J. Zembrzuska and T. Jesionowski, *Sci. Total Environ.*, 2018, **612**, 1223–1233.

52 S. K. Ali, M. Imran, O. Hakami, T. Zelai, A. A. Alamri, K. S. Ismail, M. Sharma, A. Ansari and M. S. Rashid, *Eur. Phys. J. Plus*, 2025, **140**, 24.